

# Visualizing Poiseuille flow of hydrodynamic electrons

<https://doi.org/10.1038/s41586-019-1788-9>

Received: 26 May 2019

Accepted: 11 October 2019

Published online: 4 December 2019

Joseph A. Sulpizio<sup>1,8</sup>, Lior Ella<sup>1,8</sup>, Asaf Rozen<sup>1,8</sup>, John Birkbeck<sup>2,3</sup>, David J. Perello<sup>2,3</sup>, Debangha Dutta<sup>1</sup>, Moshe Ben-Shalom<sup>2,3,4</sup>, Takashi Taniguchi<sup>5</sup>, Kenji Watanabe<sup>5</sup>, Tobias Holder<sup>1</sup>, Raquel Queiroz<sup>1</sup>, Alessandro Principi<sup>2</sup>, Ady Stern<sup>1</sup>, Thomas Scaffidi<sup>6,7</sup>, Andre K. Geim<sup>2,3</sup> & Shahal Ilani<sup>1\*</sup>

Hydrodynamics, which generally describes the flow of a fluid, is expected to hold even for fundamental particles such as electrons when inter-particle interactions dominate<sup>1</sup>. Although various aspects of electron hydrodynamics have been revealed in recent experiments<sup>2–11</sup>, the fundamental spatial structure of hydrodynamic electrons—the Poiseuille flow profile—has remained elusive. Here we provide direct imaging of the Poiseuille flow of an electronic fluid, as well as a visualization of its evolution from ballistic flow. Using a scanning carbon nanotube single-electron transistor<sup>12</sup>, we image the Hall voltage of electronic flow through channels of high-mobility graphene. We find that the profile of the Hall field across the channel is a key physical quantity for distinguishing ballistic from hydrodynamic flow. We image the transition from flat, ballistic field profiles at low temperatures into parabolic field profiles at elevated temperatures, which is the hallmark of Poiseuille flow. The curvature of the imaged profiles is qualitatively reproduced by Boltzmann calculations, which allow us to create a ‘phase diagram’ that characterizes the electron flow regimes. Our results provide direct confirmation of Poiseuille flow in the solid state, and enable exploration of the rich physics of interacting electrons in real space.

The notion of viscosity arises in hydrodynamics to describe the diffusion of momentum in a fluid under the application of shear stress. When scattering between constituent fluid particles becomes dominant, viscosity manifests as an effective frictional force between fluid layers. The hallmark of such hydrodynamic transport in a channel is a parabolic, or Poiseuille, velocity flow profile, which typifies familiar phenomena like water flowing through a pipe. Electron flow has long been predicted<sup>1</sup> to undergo hydrodynamic transport when the rate of momentum-conserving Coulomb scattering between electrons exceeds that of momentum-relaxing scattering from impurities, boundaries and phonons<sup>2,13,14</sup>. The implications of a dominant viscous force on electronic flow have been studied in a range of theoretical work<sup>15–21</sup>. While initial efforts were based on linearized Navier–Stokes equations, describing electron hydrodynamics in the context of diffusive transport<sup>14,18–20,22</sup>, there is an evolving understanding that a central part of the physics is the emergence of hydrodynamics from ballistic flow<sup>3,6,7,10,23–28</sup>. Reaching the hydrodynamic regime experimentally requires materials of high purity so that Ohmic transport can be minimized, which is now possible in a growing number of high-mobility systems. Indeed, recent experiments have demonstrated the existence of negative non-local resistance<sup>3,7</sup>, superballistic flow<sup>6</sup>, signatures of Hall viscosity<sup>9,11</sup>, breakdown of the Wiedemann–Franz law<sup>4,8</sup>, and anomalous scaling of resistance

with channel width<sup>5</sup>, all phenomena associated with hydrodynamic electron flow. Yet the direct observation of the fundamental Poiseuille flow profile has remained elusive.

In this work, we provide the first, to our knowledge, spatial imaging of Poiseuille flow of hydrodynamic electrons, as well as the evolution from ballistic to hydrodynamic flow. We use a scanning carbon nanotube single-electron transistor (SET) to non-invasively image maps of the longitudinal and Hall voltage of electrons flowing through high-mobility graphene/hexagonal boron nitride (hBN) channels<sup>12</sup>. By varying the carrier density (degenerate regime away from charge neutrality) and temperature, we tune the two relevant length scales controlling electron flow: the momentum-relaxing mean free path, set by electron-impurity and electron–phonon scattering, and the momentum conserving mean free path, set by electron–electron interactions. We find that the spatial profile of the Hall field across the channel is key to distinguishing the evolution from ballistic into hydrodynamic flow. At low temperatures, we observe flat profiles associated with ballistic flow. At higher temperatures the profiles become parabolic, with curvature approaching that of ideal Poiseuille flow. Overall, we find that Boltzmann kinetic equations qualitatively reproduce our observations, although at the highest temperatures they underestimate the curvature of the Hall field profiles. Finally, we show that this

<sup>1</sup>Department of Condensed Matter Physics, Weizmann Institute of Science, Rehovot, Israel. <sup>2</sup>School of Physics and Astronomy, University of Manchester, Manchester, UK. <sup>3</sup>National Graphene Institute, University of Manchester, Manchester, UK. <sup>4</sup>Department of Physics and Astronomy, Tel-Aviv University, Tel Aviv, Israel. <sup>5</sup>National Institute for Materials Science, Tsukuba, Japan.

<sup>6</sup>Department of Physics, University of California, Berkeley, CA, USA. <sup>7</sup>Department of Physics, University of Toronto, Toronto, Ontario, Canada. <sup>8</sup>These authors contributed equally: J. A. Sulpizio, L. Ella, A. Rozen. \*e-mail: shahal.ilani@weizmann.ac.il

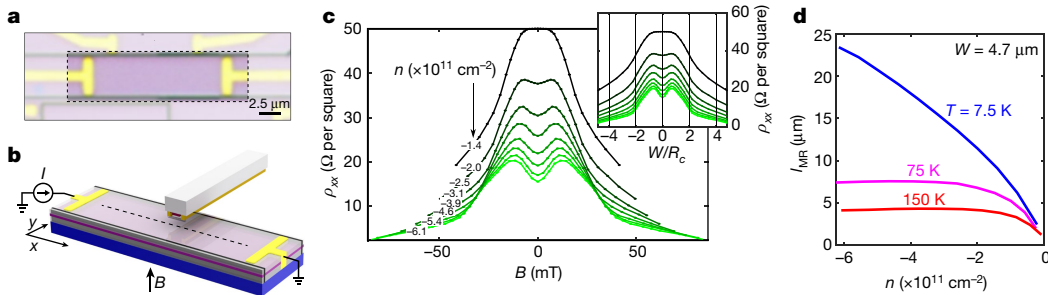


**Fig. 1 | Overview of graphene channel device and imaging of magnetoresistance.** **a**, Optical image of graphene channel device used for imaging electron flow, consisting of a high-mobility monolayer of graphene sandwiched between hBN layers (purple) and electrical contact electrodes (yellow) on top of the conducting Si/SiO<sub>2</sub> back gate. The dark lines are etched walls that define a channel of width  $W = 4.7 \mu\text{m}$  and length  $L = 15 \mu\text{m}$  (outlined with dashed box; scale bar,  $2.5 \mu\text{m}$ ). **b**, Rendering of scanning SET imaging performed in experiments. The nanotube-based SET is positioned at the end of a scanning probe cantilever, and is rastered across the channel (graphene in purple, sandwiched between hBN layers atop a Si/SiO<sub>2</sub> substrate in blue) to locally image the potential generated by the electrical current  $I$  in a perpendicular magnetic field  $B$ . **c**, Magnetoresistance of graphene channel at a temperature of  $T = 7.5 \text{ K}$ , antisymmetrized in  $B$ , imaged non-invasively with

scanning SET. The SET is scanned along the centreline of the channel (black dashed line in **b**) to image the potential drop  $\Delta\phi$  in order to extract the longitudinal resistance  $\rho_{xx} = W \frac{\Delta\phi}{\Delta I}/I$  as a function of magnetic field  $B$  for different charge carrier densities  $n$  (black curve is low density, high density in green; numbers label the density of each curve). Inset, the same  $\rho_{xx}$  data plotted as a function of  $W/R_c$ , which is proportional to  $B$  (see text). At high density, the magnetoresistance curves show a double-peaked structure, indicating ballistic transport with diffusive walls (see Methods). **d**, Momentum-relaxing mean free path  $l_{\text{MR}}$  in the bulk of the graphene channel as a function of carrier density for several temperatures. The SET is maintained at liquid helium temperature throughout all measurements<sup>11</sup>. The value of  $l_{\text{MR}}$  is deduced from  $\rho_{xx}(B)$  and is described in Methods, which also presents the associated mobility (Extended Data Fig. 1).

curvature is the distinctive metric for characterizing the different flow regimes, allowing us to construct a phase diagram and map the regions explored by the experiment.

The devices we studied are high-mobility monolayer graphene/hBN heterostructures patterned into channels of various lengths,  $L$ , and widths,  $W$ . Below we present data from a device with  $W = 4.7 \mu\text{m}$  and  $L = 15 \mu\text{m}$  (Fig. 1a), but similar results have been obtained for a device with a different width, aspect ratio, and etched boundaries (see Methods and Extended Data Fig. 5).

We first perform the scanning analogue<sup>12</sup> of transport measurements of longitudinal resistivity,  $\rho_{xx}$ . Flowing current  $I$  through the channel and imaging the potential produced by the flowing electrons,  $\phi(x)$ , along the centreline (dashed line in Fig. 1b) yields  $\rho_{xx} = W \frac{d\phi}{dx}/I$ . Figure 1c shows  $\rho_{xx}$  as a function of perpendicular magnetic field,  $B$ , for various carrier densities,  $n$ , at a temperature of  $T = 7.5 \text{ K}$ . Notably, with increasing  $|n|$ ,  $\rho_{xx}$  evolves from a single- to double-peaked structure. This is a well known signature of ballistic electron transport ( $l_{\text{MR}} > W$ , where  $l_{\text{MR}}$  is the momentum-relaxing mean free path), when scattering at the walls is diffusive<sup>5,29</sup> (see Methods and Extended Data Fig. 2). The  $B$  dependence of  $\rho_{xx}$  is set by the ratio of  $W$  and the cyclotron radius,  $R_c = \frac{\hbar \sqrt{n|n|}}{eB}$  ( $\hbar$  is the reduced Planck constant and  $e$  is the electron charge). For  $|W/R_c| > 2$ , backscattering is strongly suppressed, and Boltzmann theory predicts<sup>24</sup> that  $\rho_{xx}$  is determined primarily by bulk scattering (with correction proportional to  $|W/R_c|^{-1}$ ), allowing us to estimate  $l_{\text{MR}}$  (see Methods and Extended Data Fig. 1). Figure 1d plots the extracted  $l_{\text{MR}}$  as a function of  $n$  at several different temperatures. For  $T = 7.5 \text{ K}$ ,  $l_{\text{MR}}$  exhibits the expected  $|n|$ -dependence, while at  $T = 75 \text{ K}$  and  $150 \text{ K}$ ,  $l_{\text{MR}}$  displays a characteristic flat density dependence due to the addition of phonon scattering<sup>30</sup>.

We now turn to the Hall voltage profiles, which are fundamentally related to the current flow profiles of electrons in the channel. We restrict all subsequent analysis to the bulk of the channel ( $|y/W| < 0.3$ ), in which the convolution of the potential jump near the channel edge with the point spread function of our SET due to the imaging height ( $h \approx 880 \text{ nm}$ ) is negligible (Fig. 2a, b). In the Ohmic regime ( $l_{\text{MR}} \ll W$ ), there is a local relation between the  $y$ -component of the Hall field,  $E_y = dV_{\text{Hall}}/dy$  (where  $V_{\text{Hall}}$  is the local Hall voltage), and the current density parallel to the channel axis,  $j_x$ , given by  $E_y = (B/ne)j_x$ . In the hydrodynamic regime, where  $l_{\text{ee}} < W$  (where  $l_{\text{ee}}$  is the electron-electron scattering

length), the current density is predicted to be parabolic, leading to an analogous relation<sup>31</sup> (see Methods):

$$E_y = \frac{B}{ne} \left( j_x + \frac{1}{2} l_{\text{ee}}^2 \partial_y^2 j_x \right) \quad (1)$$

Deep in the hydrodynamic regime, where  $l_{\text{ee}}/W \ll 1$ , the local relation between  $E_y$  and  $j_x$  is recovered to a good approximation. Imaging  $E_y(y)$  in these regimes therefore effectively images the current distribution,  $j_x(y)$ . In the ballistic regime, this relation breaks down, leading to a fundamentally different  $E_y$  profile. As we show,  $E_y$  is then a key observable for distinguishing between ballistic and hydrodynamic flows. Figure 2c shows the potential along  $y$  measured at small magnetic fields  $B = \pm 12.5 \text{ mT}$ , antisymmetrized in  $B$ , to yield the Hall voltage profile  $V_{\text{Hall}}(y) = \frac{1}{2} [\phi(y, B) - \phi(y, -B)]$  where  $T = 7.5 \text{ K}$  and  $n = -1.5 \times 10^{11} \text{ cm}^{-2}$ . Note that  $B$  is small enough that the flow remains semiclassical (Landau level filling factor  $v \gg 100$  and  $\hbar\omega_c \ll k_B T$ , where  $\omega_c$  is the cyclotron frequency and  $k_B$  is the Boltzmann constant). The  $E_y(y)$  profiles are obtained by numerically differentiating the imaged  $V_{\text{Hall}}(y)$  profiles.

We now observe how electron-electron interactions affect the Hall field profiles by comparing imaging at different temperatures:  $T = 7.5 \text{ K}$  in Fig. 2e, and  $T = 75 \text{ K}$  in Fig. 2f. While increased temperature should increase the electron-electron scattering rate (decrease  $l_{\text{ee}}$ ) it also increases electron-phonon scattering (decreases the electron-phonon mean free path,  $l_{\text{ph}}$ ) and correspondingly reduces  $l_{\text{MR}} = (l_{\text{imp}}^{-1} + l_{\text{ph}}^{-1})^{-1}$ , where  $l_{\text{imp}}$  is the impurity scattering mean free path. To best isolate the influence of  $l_{\text{ee}}$ , we therefore maintain a nearly constant  $l_{\text{MR}}$  across the different temperatures by tuning the carrier density between the measurements (circles in Fig. 2d; see legend for details). Notably, the imaged profile at  $T = 7.5 \text{ K}$  is flat across the bulk of the channel (Fig. 2e). In contrast, the profile at  $T = 75 \text{ K}$  is strongly parabolic (Fig. 2f). The dramatic difference in curvature between these profiles becomes more apparent when we image the full two-dimensional maps of the Hall field (within the black box in Fig. 2a), demonstrating that the profiles are independent of position along the channel (Fig. 2g, h). All measurements are performed at small enough magnetic field ( $W/R_c = 1.3$ ) to minimally influence the profiles, as well as low voltage bias across the channel to avoid electron heating (see Methods and Extended Data Figs. 3, 4).

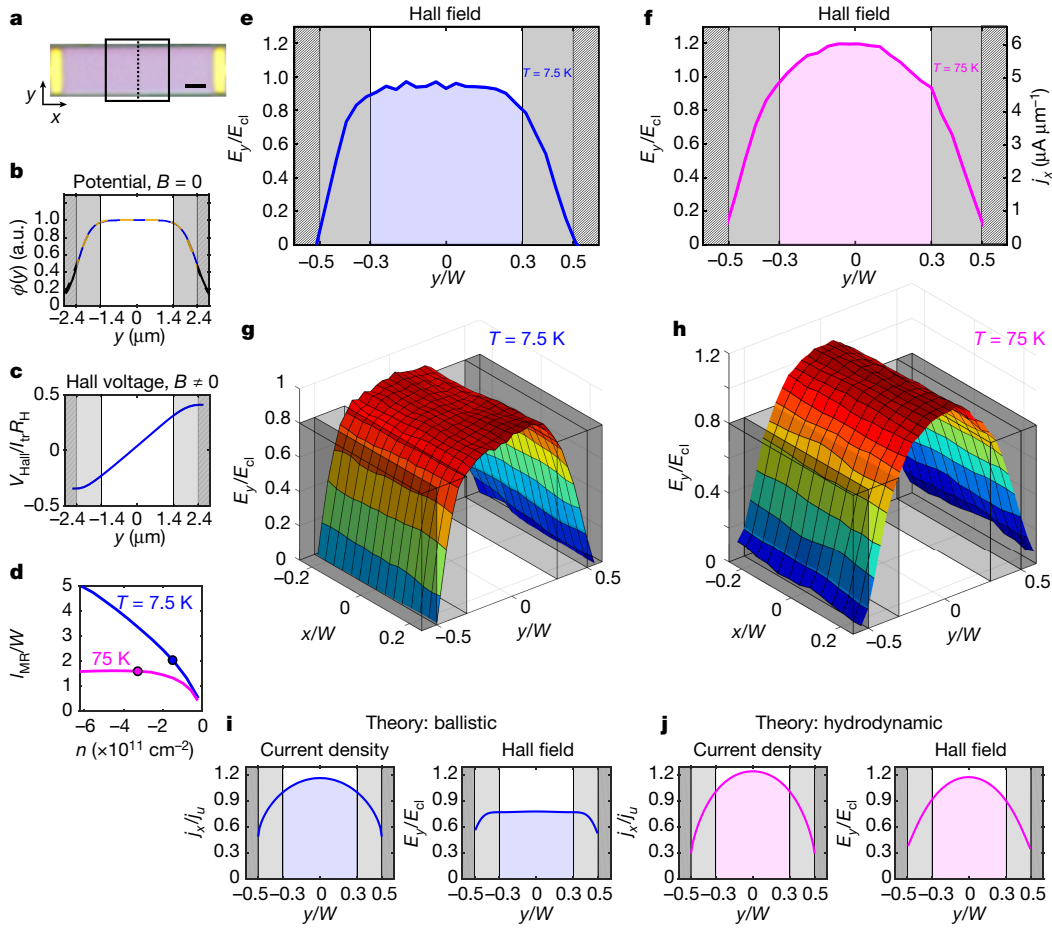


**Fig. 2 | Imaging ballistic and Poiseuille electron flow profiles.** **a**, Graphene channel with overlay indicating the region over which flow profiles are imaged. One-dimensional profiles are taken along the dashed line and two-dimensional profiles are imaged across the region enclosed by the black box (scale bar, 2.5  $\mu\text{m}$ ). **b**, Potential of flowing electrons,  $\phi$ , as a function of the y coordinate (dashed line in **a**) imaged at  $B = 0$  (blue curve,  $T = 7.5\text{ K}$ ). The dashed yellow curve is a boxcar function convolved with the point spread function of our SET measurement, determined primarily by the height of our SET detector above the graphene during the scan. Grey-shaded regions ( $0.3 < |y/W| < 0.5$ ) indicate where the smearing of the steps at the edges due to the finite spatial resolution has a non-negligible contribution. **c**, Imaged Hall voltage,  $V_{\text{Hall}}$ , from antisymmetrizing measurements taken at field  $B = \pm 12.5\text{ mT}$ ,  $n = -1.5 \times 10^{11}\text{ cm}^{-2}$  and  $T = 7.5\text{ K}$ . Normalization  $I_{\text{tr}}R_{\text{H}} = 470\text{ }\mu\text{V}$ . **d**,  $I_{\text{MR}}$  from Fig. 1d, but now normalized by  $W$ . Dots indicate the carrier densities of the profile imaging in all subsequent panels, where  $n = -1.5 \times 10^{11}\text{ cm}^{-2}$  at 7.5 K and  $n = -3.1 \times 10^{11}\text{ cm}^{-2}$  at

75 K, chosen such that  $I_{\text{MR}}$  is nearly equal for both temperatures. **e**, The Hall field,  $E_y$ , at  $T = 7.5\text{ K}$ , from measurements at  $B = \pm 12.5\text{ mT}$ , obtained by numerical differentiation of  $V_{\text{Hall}}$  with respect to  $y$ , normalized by the classical value  $E_{\text{cl}} = (B/ne)/W = 91\text{ V m}^{-1}$ . **f**,  $E_y$  at  $T = 75\text{ K}$ , from measurements at  $B = \pm 18.0\text{ mT}$ , with  $E_{\text{cl}} = 162\text{ V m}^{-1}$ . The right y axis converts the field to units of current density by scaling with  $ne/B$ . **g**, Two-dimensional map of  $E_y$  taken over the boxed region in **a** at  $T = 7.5\text{ K}$ . **h**, Two-dimensional map of  $E_y$  at  $T = 75\text{ K}$ . **i,j**, Calculation of the current density  $j_x$  (normalized by  $j_u = I/W = 2\text{ A m}^{-1}$  in **i** and  $5.4\text{ A m}^{-1}$  in **j**), and the Hall field  $E_y/E_{\text{cl}}$  based on the Boltzmann theory with values of  $I_{\text{MR}}$  and  $I_{\text{ee}}$  corresponding to the experimental data in **e** and **f**. In **i**, the values used are  $I_{\text{MR}}/W = 2$  and  $I_{\text{ee}}/W = 4.3$ , whereas for **j**,  $I_{\text{MR}}/W = 1.4$  and  $I_{\text{ee}}/W = 0.16$ . The calculated profiles are convolved with the point spread function of the SET for direct comparison with the experiment. The current density appears parabolic in both the hydrodynamic and ballistic regimes, whereas the  $E_y$  profile is relatively flat in the ballistic regime and parabolic in the hydrodynamic regime.

One naively expects the current density profile,  $j_x(y)$ , to be flat for ballistic flow and parabolic for hydrodynamic Poiseuille flow. However, a full Boltzmann theoretical calculation of the profiles of  $j_x$  and  $E_y$  including  $I_{\text{MR}}$  (Fig. 2i,j and Methods) reveals that this is not the case. The  $j_x$  profile, even deep in the ballistic regime ( $I_{\text{MR}}/W \gg 1$ ), is not flat (see Methods and Extended Data Fig. 8). Figure 2i plots the  $j_x$  profile calculated for  $I_{\text{MR}}/W = 2$  and  $I_{\text{ee}}/W = 4.3$ , consistent with our measurements at  $T = 7.5\text{ K}$ , showing that  $j_x$  has large curvature. In fact, the Boltzmann theory predicts a strongly curved  $j_x$  profile even for much larger  $I_{\text{MR}}/W$ , showing that the ballistic  $j_x$  profile is not qualitatively different from its hydrodynamic counterpart (an example calculated for  $I_{\text{MR}}/W = 1.4$  and  $I_{\text{ee}}/W = 0.16$  is shown in Fig. 2j), and is therefore a weak marker for the emergence of electron hydrodynamics. In contrast, the Boltzmann theory shows that the  $E_y$  profile differs markedly between ballistic and hydrodynamic flows, making it a way of distinguishing these regimes. In the ballistic regime  $E_y$  is flat (Fig. 2i), and can even

become negatively curved if  $I_{\text{MR}}/W$  is increased further, while in the Poiseuille regime  $E_y$  is positively curved (Fig. 2j).

The  $E_y$  profile in Fig. 2j is calculated to best fit our measurements at  $T = 75\text{ K}$  (Fig. 2f) with a Knudsen number of  $\text{Kn} = I_{\text{ee}}/W = 0.16$ . This is consistent with hydrodynamic electron flow in which  $I_{\text{ee}}$  is the smallest length scale in the system, in agreement with previous transport measurements<sup>3,6,11</sup>. The  $j_x$  and  $E_y$  profiles calculated for these parameters (Fig. 2j) are similarly curved (deviation scales as  $(I_{\text{ee}}/W)^{-2}$ , consistent with equation (1)), showing that the imaged  $E_y$  profile (Fig. 2f) approximates the actual Poiseuille  $j_x$  profile to within 5% (see the right y axis). The theoretical  $j_x$  profile corresponding to the  $T = 75\text{ K}$  measurement does not reach zero at the walls. Extrapolating this profile to zero yields an estimated slip length<sup>19,32</sup> of  $l_{\text{slip}} \approx 500\text{ nm}$ .

Having imaged the emergence of Poiseuille flow at increased temperatures, we now explore its carrier density dependence. For a linearly dispersing spectrum, Fermi liquid theory predicts  $I_{\text{ee}} \propto E_F/T^2 \propto \sqrt{|n|}/T^2$

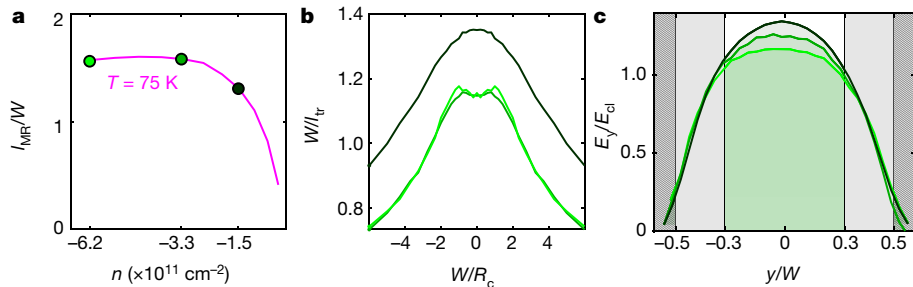


**Fig. 3 | Carrier density dependence of hydrodynamic electron flow profiles.** **a**,  $I_{\text{MR}}/W$  for  $T=75\text{ K}$  taken from Fig. 1d, with dots indicating values of  $n$  corresponding to experiments in subsequent panels. Between the green dots,  $I_{\text{MR}}$  is practically independent of  $n$  owing to the combination of phonon and impurity scattering. **b**, Comparison of magnetoresistance in units of the inverse transport mean free path  $W/l_{\text{tr}}$ , where for Dirac electrons  $l_{\text{tr}}(B)=h/[2e^2(\pi|n|)^{1/2}\rho_{xx}(B)]$  (where  $h$  is Planck's constant), at  $T=75\text{ K}$  for several

values of  $n$  indicated by the colour of the curve (corresponding to dots in **a**). The two green curves at higher  $|n|$  exhibit nearly indistinguishable magnetotransport. **c**,  $E_y/E_{\text{D}}$  profiles imaged for the same values of  $n$  as in **b** as indicated by colour ( $W/R_c=1.3$  for each curve, with  $B=\pm 25.4\text{ mT}$ ,  $18.5\text{ mT}$  and  $12.5\text{ mT}$  for  $n=-6.2\times 10^{11}\text{ cm}^{-2}$ ,  $-3.3\times 10^{11}\text{ cm}^{-2}$  and  $-1.5\times 10^{11}\text{ cm}^{-2}$ , respectively), demonstrating the monotonic increase of curvature with decreasing  $|n|$ .  $E_y^{\text{cl}}$  is the bulk value for the classical Hall field,  $(B/ne)/W$ .

(where  $E_F$  is the Fermi energy), and so a variation of the flow profiles with  $n$  is expected. Varying  $n$ , however, will generically also change  $I_{\text{MR}}$ , possibly masking the relatively weak  $\sqrt{|n|}$ -dependence of  $I_{\text{ee}}$ . Fortunately, at elevated temperatures there is a range of  $n$  over which  $I_{\text{MR}}$  remains nearly constant owing to the compensating effects of phonon and impurity scattering (between green dots in Fig. 3a,  $T=75\text{ K}$ ). In fact, the magnetoresistance at two substantially different densities (Fig. 3a, green dots) is nearly identical (Fig. 3b, green curves), implying that from transport measurements alone it is impossible to distinguish between electron flows at these densities (see Methods and Extended Data Fig. 6). However, the corresponding imaged  $E_y$  profiles (Fig. 3c, green curves)

are markedly different, varying in curvature by about 50%, which reflects the variation in  $I_{\text{ee}}$ . This result again highlights that  $E_y$  is a sensitive indicator for hydrodynamics. At even lower  $|n|$  (black dot, Fig. 3a)  $I_{\text{MR}}$  drops and both magnetoresistance (Fig. 3b, black curve) and the  $E_y$  profile (Fig. 3c, black curve) change as compared to higher densities.

We now systematically investigate how the curvature of  $E_y$  varies over a broader range of  $n$  and  $T$ . For each  $n$  and  $T$  we image the  $E_y$  profile, fit it to the form  $E_y(y)=ay^2+c$  for  $|y/W|<0.3$ , and extract the normalized curvature  $\kappa=-(a/c)(W/2)^2$  ( $\kappa=0$  for a flat profile and  $\kappa=1$  for an ideal parabolic Poiseuille profile, reaching zero at the walls). Figure 4a plots the measured  $\kappa$  as a function of  $n$  for  $T=7.5\text{ K}$ ,  $T=75\text{ K}$  and  $T=150\text{ K}$ .

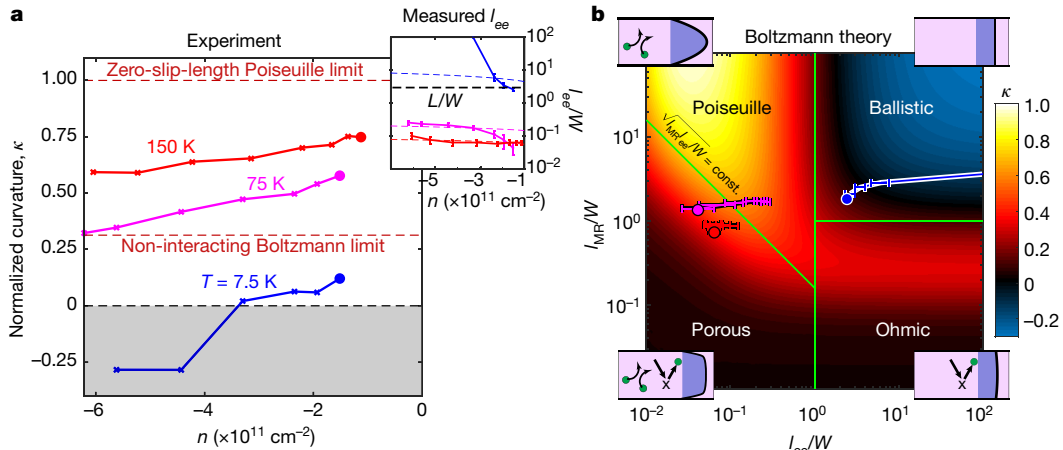


**Fig. 4 | Curvature of the imaged  $E_y$  profiles and phase diagram of electron flow regimes.** **a**, Normalized curvature,  $\kappa$ , of the imaged  $E_y$  profiles as a function of  $n$  and  $T$  as described in the main text (data points marked by crosses). Dashed red lines mark the maximal curvature obtained for non-interacting electrons based on Boltzmann calculations, and also the curvature of the ideal Poiseuille flow with zero slip length. Inset,  $I_{\text{ee}}$  at the values of  $n$  and  $T$  from the experiment (solid lines), determined by comparing the imaged  $E_y$  profiles to those calculated using the Boltzmann equations (error bars correspond to the standard deviation of  $I_{\text{ee}}$ , computed by least-squares fitting of Boltzmann calculations to experimental data). The coloured dashed lines are the corresponding predictions for  $I_{\text{ee}}$  based on many-body calculations for monolayer graphene<sup>33</sup>. The dashed black line marks the length of the device  $L$  (normalized by  $W$ ), above which the Boltzmann theory for an infinitely long channel can no longer predict  $I_{\text{ee}}$ . **b**, Phase diagram of electron flow as obtained from  $\kappa$ , calculated by Boltzmann theory (colour scale) as a function of  $I_{\text{MR}}/W$  and  $I_{\text{ee}}/W$ . The curvature values are determined by convolving the calculated profiles with the point spread function of the experiment at the same finite magnetic fields as in the experiment ( $W/R_c=1.3$ ) for best comparison. The different electron flow regimes are labelled (ballistic, Ohmic, Poiseuille and

porous) together with illustrations of the relevant scattering mechanisms. Electrons are drawn as green circles, and  $E_y$  profiles are schematically drawn in purple. In the ballistic regime, the  $E_y$  profile is flat or even negatively curved (the magnitude of negative curvature is limited by the nonzero magnetic field). In the Ohmic regime, electrons scatter primarily from impurities/phonons (drawn as crosses), and the  $E_y$  profile can be gently curved. In the Poiseuille regime, electrons primarily scatter from other electrons, leading to a strongly parabolic  $E_y$  profile. In the porous regime, both electron scattering from impurities and phonons and electron-electron scattering have a prominent role, resulting in an  $E_y$  profile that is gently curved in the middle of the channel and reaches zero over a distance of the order of  $D_v=\frac{1}{2}\sqrt{l_{\text{MR}}l_{\text{ee}}}$  from the walls. The green lines mark the transitions between the different regimes: ballistic to Ohmic at  $I_{\text{MR}}/W=1$ , transition to hydrodynamics  $I_{\text{ee}}/W=1$ , and transition from Poiseuille to porous at  $D_v/W\approx 1$ . In the Poiseuille regime the profiles can reach a maximum curvature of  $\kappa=1$ . The overlaid blue, purple and red paths correspond to the values of  $I_{\text{MR}}$  and  $I_{\text{ee}}$  (same error bars as in the inset of **a**) at  $T=7.5\text{ K}$ ,  $T=75\text{ K}$  and  $T=150\text{ K}$ , respectively, from the experimental traces in **a**, with the dots indicating the lowest density.

At  $T = 7.5$  K we find that  $\kappa$  is close to zero, and even becomes negative at high density. We further observe that the value of  $\kappa$  monotonically increases with increasing  $T$  and decreasing  $|n|$ , with the measured curvature approaching the ideal Poiseuille value at the highest  $T$  and lowest  $|n|$ .

To demonstrate the relation between the curvature of the  $E_y$  profiles and the flow regime more quantitatively, we plot in Fig. 4b a phase diagram of the flow based on  $\kappa$  calculated using the Boltzmann theory as a function of the two length scales that control the physics:  $l_{\text{MR}}/W$  and  $l_{\text{ee}}/W$ . The phase space is demarcated into four regions: Ohmic, ballistic, Poiseuille and porous, the last two of which are hydrodynamic. In the Ohmic regime the curvature is small, peaking when  $l_{\text{MR}}/W \approx 0.25$ . In the ballistic regime, where  $l_{\text{MR}}/W > 1$ ,  $\kappa$  is governed by the reciprocal sum  $\left(\frac{1}{l_{\text{ee}}} + \frac{1}{l_{\text{MR}}}\right)^{-1}$ , and even becomes negative (see Fig. 4a at  $T = 7.5$  K). In the left half of the phase diagram ( $l_{\text{ee}}/W < 1$ ), the flow is hydrodynamic, and is either Poiseuille (top left) or porous (bottom left) in character. The transition occurs when the so-called ‘Gurzhi’ length,  $D_v = \frac{1}{2} \sqrt{l_{\text{ee}} l_{\text{MR}}}$ , crosses  $W$ . In the porous regime ( $D_v < W$ ), named in analogy to water flow through porous media, both  $l_{\text{MR}}$  and  $l_{\text{ee}}$  can be smaller than  $W$ . Here,  $\kappa$  is low as in the Ohmic regime, but electron–electron interactions cause a sharp drop of  $E_y$  at the walls. In the Poiseuille regime ( $D_v > W$ ),  $\kappa$  increases substantially, approaching  $\kappa = 1$ , with the parabolic profiles of both  $E_y$  and  $j_x$  reaching zero at the walls (see Methods and Extended Data Fig. 8).

We now quantitatively compare the imaged  $E_y$  profiles at each density and temperature against the Boltzmann theory. Using the  $l_{\text{MR}}$  presented in Fig. 1d, we fit the entire Boltzmann profiles to our imaged profiles to determine the  $l_{\text{ee}}$  that gives the best match. The extracted values of  $l_{\text{ee}}$  (solid lines in the inset of Fig. 4a) are in close agreement with the many-body calculation for monolayer graphene<sup>33</sup> (see dashed lines in the inset of Fig. 4a), exhibiting the predicted decrease of  $l_{\text{ee}}$  with decreasing  $|n|$  and increasing  $T$ . Note that once  $l_{\text{ee}}$  exceeds the length of the channel (dashed black line) the Boltzmann calculations, which assume an infinite channel, lose their predictive power. Also, although at  $T = 7.5$  K and  $T = 75$  K the Boltzmann profiles closely match the overall magnitude and curvature of the imaged  $E_y$  profiles, at  $T = 150$  K, the best-fit profiles underestimate the imaged curvature (see Methods and Extended Data Fig. 9). This is probably caused by the scattering time approximation used in the calculation, suggesting that an improved microscopic understanding of electron–electron interactions is necessary to more completely understand hydrodynamics in real electronic systems (for example, using scattering integrals that better account for energy–momentum conservation in two dimensions, such as the long-lived odd-parity Fermi surface excitation modes proposed in refs.<sup>34,35</sup>). Finally, we overlay the values of  $l_{\text{MR}}$  and  $l_{\text{ee}}$  obtained from the measurements onto Fig. 4b (coloured paths correspond to the different temperatures, dots indicate lowest densities), showing the trajectories through the phase diagram explored in the experiment. Probing deeper into the Ohmic regime is limited, as further decreasing  $l_{\text{MR}}$  requires low carrier densities where inhomogeneity near the channel edges becomes important ( $\Delta n_{\text{edges}} \approx 10^{10} \text{ cm}^{-2}$ ). Reaching deeper into the Poiseuille regime is also problematic, as the necessary higher temperature induces increased phonon scattering, resulting in  $D_v < W$ .

In conclusion, we have imaged electron flow through graphene channel devices by mapping the transverse component of the Hall electric field, which we find to be the essential element for distinguishing hydrodynamic from ballistic flow. With increasing temperature, we observe the evolution from flat ballistic profiles to curved profiles, producing images of Poiseuille electronic flow. Taken together with previous studies<sup>2–11</sup>, our experiments firmly establish the existence of an electron liquid that flows according to a universal hydrodynamic description. Our approach should enable further exploration of the physics of strongly interacting electrons upon application to other materials and topologically distinct flow geometries.

## Online content

Any methods, additional references, Nature Research reporting summaries, source data, extended data, supplementary information, acknowledgements, peer review information; details of author contributions and competing interests; and statements of data and code availability are available at <https://doi.org/10.1038/s41586-019-1788-9>.

- Gurzhi, R. N. Minimum of resistance in impurity free conductors. *Sov. Phys. JETP* **27**, 1019 (1968).
- de Jong, M. J. M. & Molenkamp, L. W. Hydrodynamic electron flow in high-mobility wires. *Phys. Rev. B* **51**, 13389–13402 (1995).
- Bandurin, D. A. et al. Negative local resistance due to viscous electron backflow in graphene. *Science* **351**, 1055–1058 (2016).
- Crossno, J. et al. Observation of the Dirac fluid and the breakdown of the Wiedemann–Franz law in graphene. *Science* **351**, 1058–1061 (2016).
- Moll, P. J. W., Kushwaha, P., Nandi, N., Schmidt, B. & Mackenzie, A. P. Evidence for hydrodynamic electron flow in PdCoO<sub>2</sub>. *Science* **351**, 1061–1064 (2016).
- Krishna Kumar, R. et al. Superballistic flow of viscous electron fluid through graphene constrictions. *Nat. Phys.* **13**, 1182–1185 (2017).
- Braem, B. A. et al. Scanning gate microscopy in a viscous electron fluid. *Phys. Rev. B* **98**, 241304 (2018).
- Gooth, J. et al. Thermal and electrical signatures of a hydrodynamic electron fluid in tungsten diphosphide. *Nat. Commun.* **9**, 4093 (2018).
- Gusev, G. M., Levin, A. D., Levinson, E. V. & Bakarov, A. K. Viscous transport and Hall viscosity in a two-dimensional electron system. *Phys. Rev. B* **98**, 161303 (2018).
- Bandurin, D. A. et al. Fluidity onset in graphene. *Nat. Commun.* **9**, 4533 (2018).
- Berdugin, A. I. et al. Measuring Hall viscosity of graphene’s electron fluid. *Science* **364**, 162–165 (2019).
- Ella, L. et al. Simultaneous imaging of voltage and current density of flowing electrons in two dimensions. *Nat. Nanotechnol.* **14**, 480–487 (2019).
- Lucas, A. & Fong, K. C. Hydrodynamics of electrons in graphene. *J. Phys. Condens. Matter* **30**, 053001 (2018).
- Levitov, L. & Falkovich, G. Electron viscosity, current vortices and negative nonlocal resistance in graphene. *Nat. Phys.* **12**, 672–676 (2016).
- Mohseni, K., Shakouri, A., Ram, R. J. & Abraham, M. C. Electron vortices in semiconductors devices. *Phys. Fluids* **17**, 100602 (2005).
- Andreev, A. V., Kivelson, S. A. & Spivak, B. Hydrodynamic description of transport in strongly correlated electron systems. *Phys. Rev. Lett.* **106**, 256804 (2011).
- Aleksiev, P. S. Negative magnetoresistance in viscous flow of two-dimensional electrons. *Phys. Rev. Lett.* **117**, 166601 (2016).
- Falkovich, G. & Levitov, L. Linking spatial distributions of potential and current in viscous electronics. *Phys. Rev. Lett.* **119**, 066601 (2017).
- Torre, I., Tomadin, A., Geim, A. K. & Polini, M. Nonlocal transport and the hydrodynamic shear viscosity in graphene. *Phys. Rev. B* **92**, 165433 (2015).
- Pellegrino, F. M. D., Torre, I., Geim, A. K. & Polini, M. Electron hydrodynamics dilemma: whirlpools or no whirlpools. *Phys. Rev. B* **94**, 155414 (2016).
- Ho, D. Y. H., Yudhistira, I., Chakraborty, N. & Adam, S. Theoretical determination of hydrodynamic window in monolayer and bilayer graphene from scattering rates. *Phys. Rev. B* **97**, 121404 (2018).
- Levchenko, A., Xie, H.-Y. & Andreev, A. V. Viscous magnetoresistance of correlated electron liquids. *Phys. Rev. B* **95**, 121301 (2017).
- Lucas, A. & Hartnoll, S. A. Kinetic theory of transport for inhomogeneous electron fluids. *Phys. Rev. B* **97**, 045105 (2018).
- Scalfidi, T., Nandi, N., Schmidt, B., Mackenzie, A. P. & Moore, J. E. Hydrodynamic electron flow and Hall viscosity. *Phys. Rev. Lett.* **118**, 226601 (2017).
- Shytov, A., Kong, J. F., Falkovich, G. & Levitov, L. Particle collisions and negative nonlocal response of ballistic electrons. *Phys. Rev. Lett.* **121**, 176805 (2018).
- Aleksiev, P. S. & Semina, M. A. Ballistic flow of two-dimensional interacting electrons. *Phys. Rev. B* **98**, 165412 (2018).
- Svintsov, D. Hydrodynamic-to-ballistic crossover in Dirac materials. *Phys. Rev. B* **97**, 121405 (2018).
- Narochnyy, B. N., Gornyi, I. V., Mirlin, A. D. & Schmalian, J. Hydrodynamic approach to electronic transport in graphene. *Ann. Phys.* **529**, 1700043 (2017).
- Masubuchi, S. et al. Boundary scattering in ballistic graphene. *Phys. Rev. Lett.* **109**, 036601 (2012).
- Wang, L. et al. One-dimensional electrical contact to a two-dimensional material. *Science* **342**, 614–617 (2013).
- Holder, T. et al. *Ballistic and hydrodynamic magnetotransport in narrow channels*. Preprint at <https://arxiv.org/abs/1901.08546> (2019).
- Kiselev, E. I. & Schmalian, J. Boundary conditions of viscous electron flow. *Phys. Rev. B* **99**, 035430 (2019).
- Principi, A., Vignale, G., Carrega, M. & Polini, M. Bulk and shear viscosities of the two-dimensional electron liquid in a doped graphene sheet. *Phys. Rev. B* **93**, 125410 (2016).
- Gurzhi, R. N., Kalinenko, A. N. & Kopeliovich, A. I. Electron-electron collisions and a new hydrodynamic effect in two-dimensional electron gas. *Phys. Rev. Lett.* **74**, 3872–3875 (1995).
- Ledwith, P., Guo, H. & Levitov, L. The hierarchy of excitation lifetimes in two-dimensional Fermi gases. *Ann. Phys.* **411**, 167913 (2019).

**Publisher’s note** Springer Nature remains neutral with regard to jurisdictional claims in published maps and institutional affiliations.

© The Author(s), under exclusive licence to Springer Nature Limited 2019

# Article

## Methods

### Device fabrication

Scanning SET devices are fabricated using a nanoscale assembly technique<sup>36</sup>. The graphene/hBN devices are fabricated using electron-beam lithography and standard etching and nanofabrication procedures<sup>3</sup> to define the channels and evaporation of Pt (see main text) and Pd/Au (Extended Data Fig. 5) to deposit contact electrodes.

### Measurements

The measurements are performed on multiple graphene devices in two separate, home-built, variable-temperature, Attocube-based scanning probe microscopes. The microscopes operate in vacuum inside liquid helium dewars with superconducting magnets, and are mechanically stabilized using Newport laminar flow isolators. A local resistive surface mount device heater is used to heat the samples under study from  $T = 7.5\text{ K}$  to  $T = 150\text{ K}$ , and a DT-670-BR bare chip diode thermometer mounted proximally to the samples and on the same printed circuit boards is used for precise temperature control. The voltage imaging technique employed is presented in ref.<sup>12</sup>. Voltages and currents (for both the SET and sample under study) are sourced using a home-built digital-to-analog converter array, and measured using a home-built, software-based audio-frequency lock-in amplifier consisting of  $1\text{ }\mu\text{V}$  accurate d.c. and a.c. sources and a Femto DPLCA-200 current amplifier and NI-9239 analog-to-digital converter. The local gate voltage of the SET is dynamically adjusted via custom feedback electronics employing a least-squares regression algorithm to prevent disruption of the SET's working point during scanning and ensure reliable measurements.

The voltage excitations applied to the graphene channels are as follows:  $<4.3\text{ mV}$  at  $T = 7.5\text{ K}$ ,  $<7.5\text{ mV}$  at  $T = 75\text{ K}$ , and  $<15\text{ mV}$  at  $T = 150\text{ K}$ , all chosen to not cause additional current heating (Extended Data Fig. 4). The magnetic fields applied are in the range  $\pm 100\text{ mT}$ .

### Determination of the momentum-relaxing mean free path

For a channel geometry of width  $W$ , as used in the experiments in this paper, the longitudinal resistivity,  $\rho_{xx}$ , reflects both the bulk resistivity of the graphene as well as scattering from the walls. To isolate the contribution from the bulk resistivity and determine the momentum-relaxing mean free path in the bulk,  $l_{\text{MR}}$ , we make use of the measured magnetoresistance. At any magnetic field we can obtain the transport mean free path from the measured  $\rho_{xx}$  via the Drude formula for Dirac electrons,  $l_{\text{tr}}(B) = h/[2e^2(\pi|n|)^{1/2}\rho_{xx}(B)]$ . In the semiclassical regime, the primary influence of a perpendicular magnetic field  $B$  is to bend the electron trajectories into cyclotron orbits of radius  $R_c = \frac{\hbar|\pi|n}{eB}$ . At small magnetic fields such that the skipping orbit diameter is larger than the channel width,  $|W/R_c| < 2$ , electrons can be efficiently backscattered in the bulk and by the walls, and thus  $l_{\text{tr}}(B)$  contains the effects of both bulk and wall scattering. On the other hand, when  $|W/R_c| > 2$ , the back-scattering from the walls is highly suppressed because a cyclotron orbit emerging from one wall cannot reach the other wall without scattering at least once in the bulk. In this regime the transport mean free path is primarily controlled by the bulk scattering length,  $l_{\text{tr}} \approx l_{\text{MR}}$ , with a small correction scaling as  $|W/R_c|^{-1}$  due to the volume participation ratio of skipping cyclotron orbits. In fact, using Boltzmann calculations of the magnetoresistance we can determine the correction factor over the entire phase space of the experiment. Extended Data Fig. 1 shows the ratio,  $l_{\text{tr}}/l_{\text{MR}}$ , calculated using Boltzmann theory (section 'Boltzmann simulations of flow profiles' in Methods), as a function of  $l_{\text{ee}}/W$  and  $l_{\text{MR}}/W$  for  $W/R_c = 3.2$ . By estimating the  $l_{\text{ee}}$  in our experiments using the  $E_y$  measurements and the Boltzmann calculations as in the main text (inset of Fig. 4a), and using  $l_{\text{tr}}$  as a zeroth-order estimate for  $l_{\text{MR}}$ , we can determine from Extended Data Fig. 1 the correction factor and obtain from our measured  $l_{\text{tr}}$  the bulk  $l_{\text{MR}}$ . Note that in the regions of the phase diagram traversed by the experiment (curves in Fig. 4b), the correction

factor is rather small and the maximum deviation of  $l_{\text{MR}}$  from  $l_{\text{tr}}$  is about 30%, so even the naive estimate,  $l_{\text{MR}} \approx l_{\text{tr}}$ , is already quite accurate.

### Diffusivity of etched channel walls in the experiment

Understanding the nature of electron scattering from the etched walls of the graphene channels is essential for both establishing the possibility of Poiseuille flow (diffusive walls are necessary for parabolic flow profiles), as well as for performing quantitative theoretical modelling of the imaging data to compare with experiment. In particular, we wish to know to what extent the scattering from the walls randomizes the momentum of an incoming electron. We quantify this property of the walls using a coefficient  $p$  that measures the probability of specular reflection, which can vary between zero and one. For perfectly specular walls,  $p = 1$ , and electrons will simply reflect off the walls in a mirror-like fashion. In the other limit, for perfectly diffusive walls,  $p = 0$ , and the momentum of the outgoing electron is completely randomized.

We use three different methods of increasing sophistication in order to extract the value of  $p$  for our channels, all of which indicate that the walls are strongly diffusive and  $p$  is nearly zero. To gain a basic intuition of the degree of diffusivity of the channel walls, we turn to a channel in which the walls for half of its length have been intentionally roughened through lithographic patterning (Extended Data Fig. 2a). This sample geometry allows us to directly compare how the voltage drops along the two different halves of the channel. We plot the voltage drop imaged along the centre of the channel in Extended Data Fig. 2b. Tellingly, we note that the voltage drops linearly across the region spanning both lithographic wall patterns (dashed red line in Extended Data Fig. 2a), with no discernible difference between the two halves. We can thus conclude that the walls of the section of the channel with the straight-line etch pattern are essentially equally as rough as the intentionally roughened section, suggesting that  $p \approx 0$ .

We next use the magnetoresistance data (see Fig. 1c) measured at  $T = 7.5\text{ K}$  to estimate  $p$ . The double-peaked structure in the magnetoresistance is a telltale sign of ballistic transport, but is only present if the channel walls are diffusive, that is,  $p < 1$ . In short, the mechanism leading to the double peaks in a ballistic channel is the bending of electron trajectories by the field which forces them to scatter off the diffusive walls. At zero magnetic field, electrons traverse in straight lines, some of which have a shallow angle with respect to the walls, and in the absence of bulk scattering can have a long mean free path. The magnetic field bends these trajectories and forces electrons to hit the walls after a distance proportional to the cyclotron radius. For specular walls, this will not affect the resistivity. However, for diffusive walls this will cause extra back-scattering, leading to the double-peaked structure. This effect is pronounced when the bulk mean free path is long. However, for a short mean free path, bulk scattering will dominate and the double peak transforms into a single peak. At the transition from single- to double-peaked, the transport mean free path at zero field obeys the relation<sup>37</sup>  $l_{\text{tr}}(B = 0) \approx W/(1 - p)$ . Extended Data Fig. 2c plots the transport mean free path as a function of magnetic field and carrier density, determined from the measured  $\rho_{xx}$  data in Fig. 1c. We see that the double-peaked structure becomes a single, broad peak as  $l_{\text{MR}}$  decreases with decreasing density,  $|n|$ . Applying the above formula, we find that  $p \approx 0 \pm 0.1$  as  $l_{\text{tr}} \approx W = 4.7\text{ }\mu\text{m}$  at the transition from single- to double-peaked spectrum.

Finally, we can independently estimate  $p$  from the scaling of  $l_{\text{tr}}(B = 0)$  as a function of density using the theoretical description for flow through a channel as a function of  $p$  developed by Molenkamp and de Jong<sup>2</sup>. We numerically solve for the fan diagram plotted in Extended Data Fig. 2d using the values of  $l_{\text{MR}}$  at  $T = 7.5\text{ K}$  from experiment, which shows how  $l_{\text{tr}}(B = 0)$  varies with carrier density  $n$ . The bold, red trace corresponds to  $p = 1$ , and is therefore identical to  $l_{\text{MR}}$  versus  $n$ , as expected for a channel with perfectly specular walls. As  $p$  is decreased from unity, the transport mean free path decreases and the curves level out, becoming rather flat at  $p = 0$ . The bold black trace in Extended Data Fig. 2d

corresponds to our experimentally measured  $l_{\text{tr}}(B=0)$  and closely matches, though very slightly undershoots the prediction for,  $p=0$ . Although the fit to the  $p=0$  theory is good, the slight mismatch suggests that, while the channel walls in the experiment are nearly fully diffusive, there may be an edge scattering mechanism at play not captured by the simple specularity coefficient used in ref.<sup>2</sup>. Nevertheless, based on the variation between curves at different  $p$ , we can estimate that for our channel  $|p| < 0.1$ , consistent with the above analyses.

We also note that although the above analysis was performed for data taken at  $T = 7.5$  K, since we expect the diffusivity of the walls only to increase as the temperature is increased, the above estimates for  $p$  are then valid for all temperatures in our experiments. Further, while one might expect  $p$  to have some variation with carrier density owing to the varying strength of p-n junctions near the channel walls, our data strongly suggest that  $p$  remains close to zero for the entire range of hole carrier densities explored in the experiment, because any deviation from zero would increase the rate of change of  $l_{\text{tr}}(B=0)$  with  $n$ , which is inconsistent with Extended Data Fig. 2d. Thus, we conclude that the etched walls of the graphene channels are effectively fully diffusive throughout the entire phase diagram of our experiment.

### Dependence of Hall field profile curvature on magnetic field

Our method for mapping the Hall field,  $E_y$ , relies on the application of a small perpendicular magnetic field,  $B$ , to produce a Hall signal that is measurable by the scanning SET. We must then verify that this measurement is in the linear response regime with respect to  $B$ , namely that  $B$  is low enough not to alter the  $E_y$  profile. Specifically, we aim to prove that the curvature of the  $E_y$  profiles,  $\kappa$ , which is a main observable in this work, is not altered by  $B$ . In Extended Data Fig. 3a, we present the curvature  $\kappa$  imaged at a constant carrier density as a function of magnetic field at three temperatures,  $T = 4$  K,  $T = 75$  K and  $T = 150$  K. The curvature is extracted as described in the main text by a parabolic fit to  $E_y$  over the centre of the channel.

We note two distinct regimes of how  $\kappa$  depends on  $B$ : for  $W/R_c > 2$ ,  $\kappa$  has a strong field dependence, whereas for  $W/R_c < 2$ ,  $\kappa$  is constant at each temperature. In the higher-field regime for  $W/R_c > 2$ , closed cyclotron orbits can fit within the width of the channel. This leads to a rich evolution of  $E_y$  profiles that are no longer simply parabolic, and is the topic of a future work. In the lower-field regime for  $W/R_c < 2$ , we see that the measured curvature is constant to within our measurement noise down to the lowest fields measured ( $W/R_c \approx 1$ ). Imaging closer to  $B = 0$  is increasingly challenging, as the signal-to-noise ratio of the measured Hall voltage decreases linearly with decreasing field. Extended Data Fig. 3b shows similar traces ( $\kappa$  versus  $W/R_c$ ) calculated using Boltzmann equations for the values of  $l_{\text{MR}}/W$  and  $l_{\text{ee}}/W$  corresponding to the experiment. We find good correspondence between the Boltzmann simulations and the experiment. Most importantly, in the low field regime for  $W/R_c < 2$ , the simulations confirm that  $\kappa$  is independent of  $B$  as observed in the experiments, and extend this observation down to  $B=0$ . Based on these results, the value of  $W/R_c = 1.3$  used for the  $E_y$  profile imaging in the experiments in the main text is justified.

Having justified experimentally and with Boltzmann simulations that the profiles are unperturbed in the low field regime  $W/R_c < 2$ , we also argue from analytic reasons why the flow profile is not expected to vary at low magnetic fields. In the hydrodynamic regime, the curvature

$$\kappa \approx \frac{W^2}{D_v^2 \sinh \left[ \frac{W}{4D_v} \right]}, \text{ where } D_v = \frac{1}{2} \sqrt{l_{\text{MR}} l_{\text{ee}}} \text{ is the Gurzhi length}^{31}.$$

For low magnetic fields the correction to  $D_v$  has the form  $1 - \frac{2l_{\text{eff}}^2}{R_c^2}$ , where  $1/l_{\text{eff}} = 1/l_{\text{MR}} + 1/l_{\text{ee}}$ . This correction goes as  $B^2$ , and will be relevant only when  $R_c$  is of the order of  $l_{\text{eff}}$ , which we are far from at  $W/R_c = 1.3$  and the values of  $l_{\text{ee}}$  and  $l_{\text{MR}}$  that we achieve in the experiment in the hydrodynamic regime. We can therefore conclude that the curvature  $\kappa$  is not dependent on magnetic field for the parameters of our experiment.

### Dependence of Hall field profile curvature on voltage excitation

In order to drive current through the graphene channel devices, we apply an oscillating bias voltage of amplitude  $V_{\text{ex}}$  between the electrical contacts to the device. This excitation can in principle induce heating of the electrons above the temperature of the cryostat, and as a result cause an increase in curvature of the Hall field profiles. While this effect can be used<sup>2</sup> instead of substrate heating, we avoid this approach here owing to the additional spurious effects it may have on the curvature. We therefore choose an excitation amplitude at each temperature that is sufficiently low to minimally influence the curvature of the imaged profiles, but still high enough to enable a robust measurement.

Extended Data Fig. 4 shows the curvature of the field profiles versus excitation amplitude  $V_{\text{ex}}$  applied to the graphene device for two temperatures,  $T = 7.5$  K in the ballistic regime (blue trace) and  $T = 75$  K in the hydrodynamic, Poiseuille regime (purple trace). The curvature is extracted by a parabolic fit to the imaged  $E_y$  Hall profile imaged across the channel at a fixed density and magnetic field as described in the main text. In the Poiseuille regime ( $T = 75$  K, density  $n = -3.3 \times 10^{11} \text{ cm}^{-2}$ ,  $W/R_c = 1.3$ ), we see that the curvature ( $\kappa \approx 0.5$ ) is essentially independent of the excitation at least up to  $V_{\text{ex}} = 11$  mV, and therefore the excitation does not influence the physics of the electron flow. In the ballistic regime ( $T = 7.5$  K,  $n = -1.5 \times 10^{11} \text{ cm}^{-2}$ ,  $W/R_c = 1.3$ ), we see a clear increase in the curvature with increasing excitation due to electron heating. Still, for an excitation of  $V_{\text{ex}} = 4.3$  mV,  $\kappa$  is nearly zero and far below the Boltzmann limit marking the transition to hydrodynamic flow. We can thus safely choose such a low excitation and robustly image ballistic electron flow through the channel, although the specific value of  $\kappa$  may still be somewhat influenced by the excitation. In the experimental data presented in the main text, for  $T = 7.5$  K, the excitation across the graphene device is chosen such that  $V_{\text{ex}} < 4.3$  mV, for  $T = 75$  K,  $V_{\text{ex}} < 7.5$  mV, and for  $T = 150$  K,  $V_{\text{ex}} < 15$  mV.

### Comparison of Hall field profile curvature for different devices

We establish the consistency of our results across a set of graphene channel devices and scanning SET probes. The measurements in this work were carried out on two separate graphene device microchips, each imaged with a different scanning microscope and different SET. This allows us to compare between measurements and establish their lack of sensitivity to details specific to a particular graphene device or experimental setup. We denote the device used throughout the main text as device A. The additional device measured, which we denote as device B, is a channel with  $W = 5 \mu\text{m}$ , and  $L = 42 \mu\text{m}$ , allowing us additionally to rule out aspect-ratio-dependent effects (aspect ratio about 3 for device A versus about 8 for device B).

To most easily compare between devices, we examine the curvature of the Hall field profiles imaged at similar SET-graphene device separations. We focus on the magnetic field dependence of the curvature at several different temperatures and densities. The results are shown in Extended Data Fig. 5. We compare first between measurements taken at  $T = 7.5$  K and  $n = -1.5 \times 10^{11} \text{ cm}^{-2}$  in device A and  $T = 4$  K and  $n = -6 \times 10^{11} \text{ cm}^{-2}$  in device B. We then repeat the same comparison, now at  $T = 75$  K for both devices and  $n = -3.3 \times 10^{11} \text{ cm}^{-2}$  for device A and  $n = -1 \times 10^{12} \text{ cm}^{-2}$  for device B. The point spread function of the SET has a similar influence on both devices, and the same valid channel region is chosen for the extraction of the curvature ( $|W/R_c| < 0.3$ ).

In the low-temperature measurement, we observe a similar overall shape in the  $W/R_c < 2$  region. The low-field curvature in device A levels off at a slightly higher value than that in device B. The latter can be attributed to the different densities, since, as observed in Fig. 4a, at  $T = 7.5$  K the curvature exhibits strong density dependence. The curvatures imaged at elevated temperature closely match each other over the full range of magnetic fields, with small residual differences that are consistent with the density dependence in Fig. 4a. This indicates that

# Article

the hydrodynamic features observed in this work are not specific to the particular graphene sample or channel dimensions being measured.

## Distinguishing electron flow regime from transport

The temperature and width dependence of the resistivity of a channel relates to one of the earliest predictions in the field of electron hydrodynamics made by Gurzhi<sup>1</sup>. Specifically, he recognized the influence of wall scattering on the total current across the transition from the ballistic regime ( $I_{ee}, I_{MR} > W$ ) to the Poiseuille regime ( $I_{ee} < \frac{W^2}{I_{ee}} < I_{MR}$ ) by increasing  $T$  and thus decreasing the viscosity, while keeping momentum-relaxing collisions negligible. As the transition is made, a decrease in resistivity is expected, and in the Poiseuille regime, one is then expected to observe  $W^3$  scaling of the conductance. It is important to note, however, that for this to occur, we must maintain throughout the crossover the more stringent condition that  $I_{MR}$  is always much greater than  $W^2/I_{ee}$  and  $I_{ee}$ . In an experiment on monolayer graphene, and with channel widths that are amenable to measurement with the current generation of scanning SETs, it is impossible to reach deeply enough into the Poiseuille regime to meet this requirement, since the increase of temperature that leads to the decrease in  $I_{ee}$  also leads to increased momentum-relaxing collisions with phonons (that is, at higher temperature the condition  $I_{MR} > W^2/I_{ee}$  breaks down).

In this situation, the question of which observables are available for measurement becomes very important. It turns out that here the curvature in  $E_y$  plays a crucial role: When one performs a Boltzmann simulation<sup>24</sup>, it can be seen that the dependence of the resistivity for the values of  $I_{ee}/W$  and  $I_{MR}/W$  corresponding to our experiment is fairly weak, and much less informative than the dependence of the curvature of  $E_y$  for the same values of these parameters. This is shown explicitly in Extended Data Fig. 6 (taken from ref.<sup>2</sup>), which plots the dependence of the effective scattering length  $L_{eff} \propto 1/\rho_{xx}$  on  $I_{ee}/W$ , and by extension, on  $T$ , for different values of  $I_{MR}/W$ . The coloured ellipses correspond to the phase space regions reached in our experiments. While the resistivity variation over the experimentally relevant parameter range is weak, the curvature in  $E_y$  can vary substantially. This stems from the fact that the curvature of the flow profile is a geometric quantity, which directly relates to the length scales in the problem. Indeed, it is possible to maintain  $I = \int j_x dy = \text{constant}$  for a fixed applied voltage while changing the curvature of  $j_x$  from fully flat to fully parabolic.

It must be emphasized here that the difficulty in extracting the flow regime from the resistivity is not a simple case of being able to measure the latter to greater precision, which would naively allow us to extract meaningful information from even a small change in the resistivity. This would indeed be the case if all the quantities that make up the total resistivity, namely  $I_{imp}$ ,  $I_{ph}$  and  $I_{ee}$ , were to have a firmly understood functional dependence on the control parameters  $n$ ,  $T$  and  $W$ . However, this is not the case in graphene, and one can construct many models that would end up giving the same nearly flat form of  $\rho_{xx}$  versus  $T$ . Therefore, even a careful fitting of data to theory would not yield definitive information.

In this context, we mention that by using a judiciously selected sample geometry, such as in ref.<sup>10</sup>, a negative minimum in the vicinity resistance  $R_v$  of a bilayer graphene sample has been observed. This minimum, however, is related to a crossover in the quantity  $I_{ee}/x$ , where  $x$  is the distance from an injection contact to an adjacent probe contact, and the minimum can be attributed to a geometric effect which is absent in a channel geometry.

## Boltzmann simulations of flow profiles

To model electron flow through the graphene channels, we employ an approach based on the Boltzmann equation<sup>2,5,38</sup> that incorporates the effects of both electron–impurity and electron–phonon scattering as well as electron–electron interactions<sup>24</sup>:

$$\partial_t f + \mathbf{v} \nabla_{\mathbf{r}} f + \frac{e}{m} (\mathbf{E} + \mathbf{v} \times \mathbf{B}) \nabla_{\mathbf{v}} f = \frac{\partial f}{\partial t} \Big|_{\text{scatt}} \quad (2)$$

where the scattering integral

$$\frac{\partial f(\mathbf{r}, \mathbf{v})}{\partial t} \Big|_{\text{scatt}} = -\frac{f(\mathbf{r}, \mathbf{v}) - n(\mathbf{r})}{\tau} + \frac{2}{v_F^2 \tau_{ee}} \mathbf{v} \cdot \mathbf{j}(\mathbf{r}) \quad (3)$$

has two contributions: one from momentum-relaxing scattering, with a rate  $1/\tau_{MR}$ , and one from momentum-conserving, electron-electron scattering, with a rate  $1/\tau_{ee}$ . This equation describes the evolution of the semiclassical occupation number  $f(\mathbf{r}, \mathbf{v})$  for a wave packet of dynamical mass  $m$  at position  $\mathbf{r}$  and velocity  $\mathbf{v}$ , where  $n(\mathbf{r}) = \langle f \rangle$ , is the local charge density,  $\mathbf{j}(\mathbf{r}) = \langle \mathbf{v} \mathbf{f} \rangle$ , is the local current density,  $\langle \dots \rangle_v$  is the momentum average, and  $\frac{1}{\tau} = \frac{1}{\tau_{MR}} + \frac{1}{\tau_{ee}}$ . For the sake of simplicity, we consider the case of a circular Fermi surface with  $\mathbf{v} = v_F \hat{\mathbf{p}}(\theta)$ , where  $\hat{\mathbf{p}}$  is the radial unit vector at angle  $\theta$  and  $v_F$  is the Fermi velocity. Mean free paths are then simply defined as  $\tau_{(MR)(ee)} = v_F \tau_{(MR)(ee)}$ . The term proportional to  $1/\tau_{ee}$  is the simplest momentum-conserving scattering term that can be written, assuming that the electrons relax to a Fermi–Dirac distribution shifted by the drift velocity<sup>39,40</sup>. This form allows for different rates of momentum-relaxing and momentum-conserving scattering while still being amenable to computation. Although first used in the context of two-dimensional electron gases with parabolic bands, it has also been applied to graphene<sup>41</sup>.

The justification for the scattering integral in equation (3) is twofold. First, we note that the experiments are always firmly in the Fermi liquid regime ( $E_F \gg k_B T$ ), where the phase space for electron–hole scattering is negligible. This is illustrated in Extended Data Fig. 7, which plots the density and temperature of the experimental  $E_y$  profiles (red, blue and purple lines) presented in Fig. 4, along with the boundary  $E_F = k_B T$  (black curve). Above this boundary lies the ambipolar electron–hole/Dirac fluid regime in which both electrons and holes are present and scattering between them must be considered. Our experiments lie far below this boundary in the degenerate Fermi liquid regime, where only carriers of a single type are present and thus scattering is unipolar.

Second, beyond the fact that our experiments are in the Fermi liquid regime, the primary difference between equation (3) and a more graphene-specific scattering integral is that in equation (3) we have neglected the enhancement of collinear scattering due to the linear spectrum, which has a logarithmic dependence on the fine structure constant<sup>41</sup>. However, for graphene encapsulated in hBN, the fine structure constant is of the order of one, and thus the enhanced collinear scattering may be neglected. Moreover, by definition, collinear scattering mainly relaxes energy and only weakly relaxes the momentum direction. Since the latter plays the dominant role in how electrons flow through a channel, it is therefore safe to neglect this correction.

We assume a sample that is of infinite length along the  $x$  axis (which is the direction of current flow), and of finite width  $W$  along the  $y$  axis. The magnetic field is applied along the  $z$  direction. Diffuse scattering at the boundaries is imposed by the following boundary condition:

$$f\left(y = +\frac{W}{2}, \pi \leq \theta < 2\pi\right) = f_{\text{boundary}} \quad (4)$$

$$f\left(y = -\frac{W}{2}, 0 \leq \theta < \pi\right) = -f_{\text{boundary}}$$

where  $f_{\text{boundary}}$  is a constant that is independent of  $\theta$  and that must be determined self-consistently. This ensures a uniform probability density for the angle at which an outgoing electron leaves a given wall, as required for completely diffuse scattering. Note that  $f_{\text{boundary}} = 0$  at zero magnetic field<sup>12</sup> but is non-zero in general. More generally, one could consider a finite degree of specularity for boundary scattering, by taking

$$\begin{aligned} f\left(y=+\frac{W}{2}, \pi \leq \theta < 2\pi\right) &= p(\theta)f\left(y=+\frac{W}{2}, -\theta\right) + f_{\text{boundary}} \\ f\left(y=-\frac{W}{2}, 0 \leq \theta < \pi\right) &= p(\theta)f\left(y=-\frac{W}{2}, -\theta\right) - f_{\text{boundary}} \end{aligned} \quad (5)$$

where  $p(\theta) \in [0, 1]$  is the degree of specularity for electrons at incidence angle  $\theta$ . Although our calculations were limited to  $p = 0$  to match the experiment (see ‘Diffusivity of etched channel walls in the experiment’ in Methods), we expect that adding a small amount of specularity would only gradually wash out both ballistic and hydrodynamic effects.

Equation (2) is supplemented by Gauss’s law with a charge density given by  $en(x)$ . The resulting integrodifferential equation is solved numerically using the method of characteristics<sup>40</sup> to invert the differential part of the equation, and an iterative method to solve the integral part.

We emphasize that the above kinetic approach does not imply a no-slip boundary condition for the current. Instead, equation (5) merely imposes randomization of the incoming momentum under boundary scattering. This condition is well suited for doped graphene (‘Diffusivity of etched channel walls in the experiment’ in Methods and ref.<sup>32</sup>) and smoothly interpolates between effectively no-slip conditions in the hydrodynamic regime and a sizable slip length for ballistic flow. For this reason, the precise value of the specularity coefficient in the calculation does not qualitatively change the solution<sup>31</sup>.

We also note that, importantly, the determination of the flow profile by means of the Boltzmann distribution function ensures that full information of the kinematics is retained. This includes exceptional trajectories in the ballistic limit. We resolve not only the long-lived trajectories which travel almost tangentially to the boundary, but also the boundary skipping orbits which impact the walls many times<sup>31</sup>.

### Relation between $E_y$ and $j_x$ in the hydrodynamic regime

In the hydrodynamic regime for a channel of bulk resistivity  $\rho_{xx}^{\text{bulk}}$  with diffusive walls, the Hall field  $E_y(y)$  across the channel at weak magnetic field calculated using the Boltzmann kinetic equation approach<sup>13,42,43</sup> is given by:

$$E_y(y) = \rho_H j_x - \frac{\frac{E_x 2l_{ee}}{R_c} \cosh\left(\frac{y}{D_v}\right)}{\cosh\left(\frac{W}{2D_v}\right)} \quad (6)$$

where  $\rho_H = B/ne$  is the Hall resistivity and  $E_x$  is the electric field along the channel. Additionally, we calculate the corresponding current density as:

$$j_x(y) = \frac{E_x}{\rho_{xx}^{\text{bulk}}} \left( 1 - \frac{\cosh\left(\frac{y}{D_v}\right)}{\cosh\left(\frac{W}{2D_v}\right)} \right) \quad (7)$$

We then note the following identity:

$$\partial_y^2 j_x = -\frac{E_x}{\rho_{xx}^{\text{bulk}}} \left( \frac{1}{D_v} \right)^2 \left( \frac{\cosh\left(\frac{y}{D_v}\right)}{\cosh\left(\frac{W}{2D_v}\right)} \right) \quad (8)$$

This allows us to substitute equation (8) into equation (6), and using

the relation  $\rho_H = \frac{\rho_{xx}^{\text{bulk}} l_{\text{MR}}}{R_c}$  we find:

$$E_y = \rho_H \left( j_x + \frac{1}{2} l_{ee}^2 \partial_y^2 j_x \right) \quad (9)$$

### Comparison of theoretical $E_y$ and $j_x$ curvature

For a long, ballistic channel, there are only two relevant parameters that determine the flow profile: the bulk mean free path normalized by the channel width  $l_{\text{MR}}/W$  and the specularity of the walls  $p$ . The case for specular walls is trivial, and the flow in the channel will be completely homogenous. The more interesting, experimentally relevant case is for diffusive walls with  $p = 0$ , where electrons flowing in the bulk are scattered with mean free path  $l_{\text{MR}}$  and electrons near the edge of the channel will encounter increased scattering by the diffusive walls. This physics alone, even without any electron–electron scattering, will produce a current density that varies from the bulk of the channel to the edges. For  $p = 0$ , the profile of  $j_x$  can then only be a function of the single parameter  $l_{\text{MR}}/W$ , where for  $l_{\text{MR}}/W \ll 1$  the flow is Ohmic and for  $l_{\text{MR}}/W > 1$  the flow is ballistic.

For a very wide channel, the current profile should be flat, as increasing  $W$  while keeping  $l_{\text{MR}}$  fixed leads to  $l_{\text{MR}}/W \ll 1$ , creating Ohmic flow. In this regime, information about the diffusive walls does not propagate substantially into the bulk, as the scattering length is much shorter than the channel width.

In the extreme ballistic regime for  $l_{\text{MR}}/W \rightarrow \infty$ ,  $j_x$  will also be flat, as an electron scattered at one wall will reach the other wall without scattering, effectively transmitting information about the diffusive walls uniformly throughout the channel. However, for non-infinite  $l_{\text{MR}}/W$ , this is no longer true, and  $j_x$  will necessarily have a curved profile. This is the experimentally relevant regime, as most published experiments on ballistic channels are done with  $l_{\text{MR}}/W$  not much greater than 1 (we reach  $l_{\text{MR}}/W \approx 5$ ). This is illustrated in Extended Data Fig. 8a, where we plot the curvature of  $j_x$  as a function of  $l_{\text{MR}}/W$ . The blue curve is based on the analytical formulas by de Jong and Molenkamp<sup>2</sup>, while the red curve is produced by a Monte Carlo electron billiards simulation. The curvature is extracted as in the main text: we fit a parabola of the form  $j_x(y) = ay^2 + c$  to the central 60% of the channel, with curvature  $\kappa = -(a/c)(W/2)^2$ . We see that the curvature of  $j_x$  can be substantial even for very large  $l_{\text{MR}}/W$ , exemplifying the difficulty in distinguishing hydrodynamic electron flow from ballistic flow based on the current profile  $j_x$ .

We further compare the phase diagram defined by the theoretical estimate for the curvature  $\kappa$  of the  $E_y$  profiles presented in Fig. 4b with the phase diagram defined by the theoretical curvature of the  $j_x$  current density profiles. This allows us to present a more complete relation between  $E_y$  and  $j_x$  for  $W/R_c = 1.3$  for each flow regime as a function of  $l_{\text{MR}}/W$  and  $l_{ee}/W$ . The phase diagrams are presented side by side in Extended Data Fig. 8b, c. The  $j_x$  curvature phase diagram is constructed similarly to the  $E_y$  phase diagram, fitting a parabola to the centre of the  $j_x$  profiles calculated from the Boltzmann model after convolution with the point spread function of the SET. Examining first the right, non-hydrodynamic half of the phase diagram, we again note the large difference between the curvature in the ballistic regime of  $E_y$  and  $j_x$ . Whereas  $E_y$  can be negatively curved,  $j_x$  is always positively curved, with high curvature throughout the ballistic regime. The crossover between the ballistic regime and the Ohmic regime is evident in both phase diagrams, although the  $j_x$  curvature simply decreases from ballistic to Ohmic, while  $E_y$  goes through a local maximum near the crossover. In the hydrodynamic regime, both phase diagrams are similar, with the curvature matching exactly in both limits of strongly Poiseuille and strongly porous hydrodynamic electron flow. This highlights the restoration of a local relation between  $E_y$  and  $j_x$ , which leads to a convergence between these quantities in the hydrodynamic regime.

### Comparisons of imaged $E_y$ profiles to simulations

To determine the best match to theory, we fit the entirety of each imaged  $E_y(y)$  profile over the range of  $|y/W| < 0.3$  to the profiles obtained from the Boltzmann calculations. As  $l_{\text{MR}}$  is already determined independently from the magnetoresistance measurements, this procedure gives us the corresponding values of  $l_{ee}$ . The fit of each profile therefore

# Article

has to match not only the curvature, but also the overall height, which is related to the total conductivity. In Extended Data Fig. 9 we present three representative imaged  $E_y$  profiles along with the best-fit Boltzmann profiles (green curves). While the theory matches the imaged profiles at  $T = 7.5$  K (blue curve) and  $T = 75$  K (purple curve) in both curvature and height, the profile at  $T = 150$  K (red curve) is clearly more curved than the best-match Boltzmann profile. As stated in the main text, this mismatch may be due to the relaxation time approximation for electron–electron interactions used in the Boltzmann calculations. Further theoretical developments are necessary to more completely explain the hydrodynamic flow profiles at higher temperatures. Still, we emphasize that this mismatch between theory and experiment does not affect the main observation in the paper, which is the observation of Poiseuille electron flow and its distinction from ballistic flow.

## Data availability

The data that support the plots and other analysis in this work are available upon request.

## Code availability

Computer code for reproducing the Boltzmann simulations and computing the electron-electron scattering length is available upon request.

36. Waissman, J. et al. Realization of pristine and locally tunable one-dimensional electron systems in carbon nanotubes. *Nat. Nanotechnol.* **8**, 569–574 (2013).

37. Thornton, T. J., Roukes, M. L., Scherer, A. & Van de Gaag, B. P. Boundary scattering in quantum wires. *Phys. Rev. Lett.* **63**, 2128–2131 (1989).
38. Dittesen, E. & Lothe, J. Theory of size effects in electrical conductivity. *Phil. Mag.* **14**, 759–773 (1966).
39. Molenkamp, L. W. & de Jong, M. J. M. Electron-electron-scattering-induced size effects in a two-dimensional wire. *Phys. Rev. B* **49**, 5038 (1994).
40. Courant, R. & Hilbert, D. *Methods of Mathematical Physics II: Partial Differential Equations* 62–131 (Wiley, 2008).
41. Kashuba, O., Trauzettel, B. & Molenkamp, L. W. Relativistic Gurzhi effect in channels of Dirac materials. *Phys. Rev. B* **97**, 2015129 (2018).
42. Gurzhi, R. N. Hydrodynamic effects in solids at low temperature. *Sov. Phys. Usp.* **11**, 255–270 (1968).
43. Alekseev, P. S. et al. Nonmonotonic magnetoresistance of a two-dimensional viscous electron-hole fluid in a confined geometry. *Phys. Rev. B* **97**, 085109 (2018).

**Acknowledgements** We thank G. Falkovich, A. Shytov, L. Levitov, D. Bandurin and R. Krishna-Kumar for discussions. We further acknowledge support from the Helmsley Charitable Trust grant, the ISF (grant number 712539), WIS-UK collaboration grant, the ERC-Cog (See-1D-Qmatter number 647413), the Deloro Award, the Minerva Foundation, and the Emergent Phenomena in Quantum Systems initiative of the Gordon and Betty Moore Foundation.

**Author contributions** J.A.S., L.E. and S.I. conceived the experiments. J.A.S., L.E., A.R., D.D. and S.I. performed the experiments. J.A.S., L.E., A.R. and S.I. analysed the data. J.B., D.J.P. and M.B.-S. fabricated the graphene devices. K.W. and T.T. supplied the hBN crystals. T.S., T.H., R.Q., A.P., A.R. and A.S. performed theoretical calculations. J.A.S., L.E. and S.I. wrote the manuscript, with input from all authors.

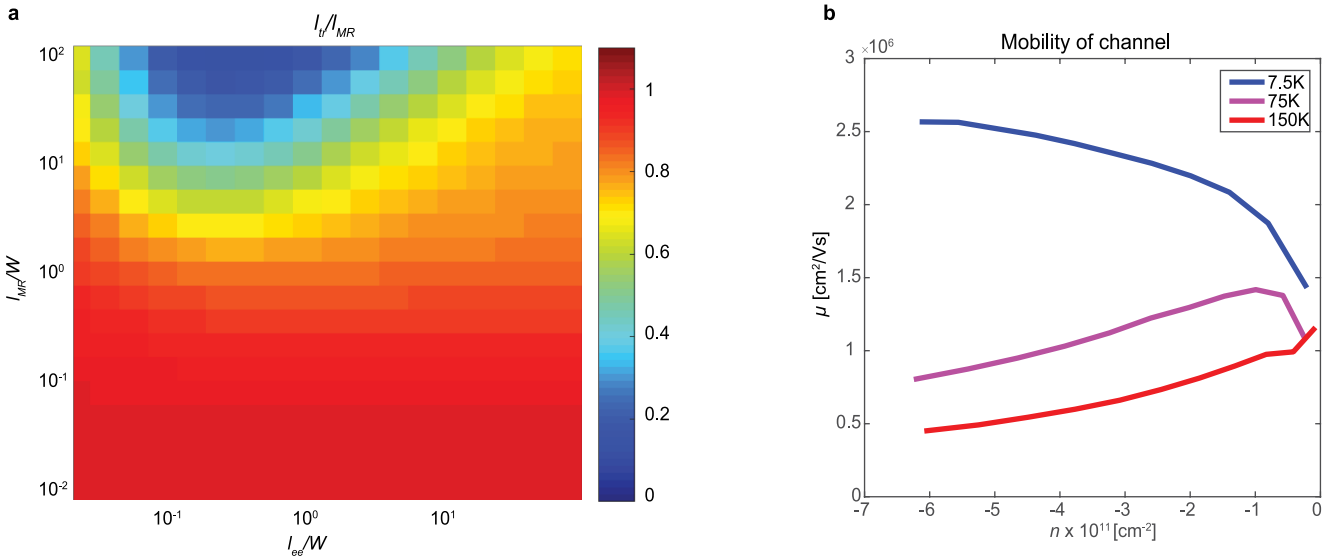
**Competing interests** The authors declare no competing interests.

### Additional information

**Correspondence and requests for materials** should be addressed to S.I.

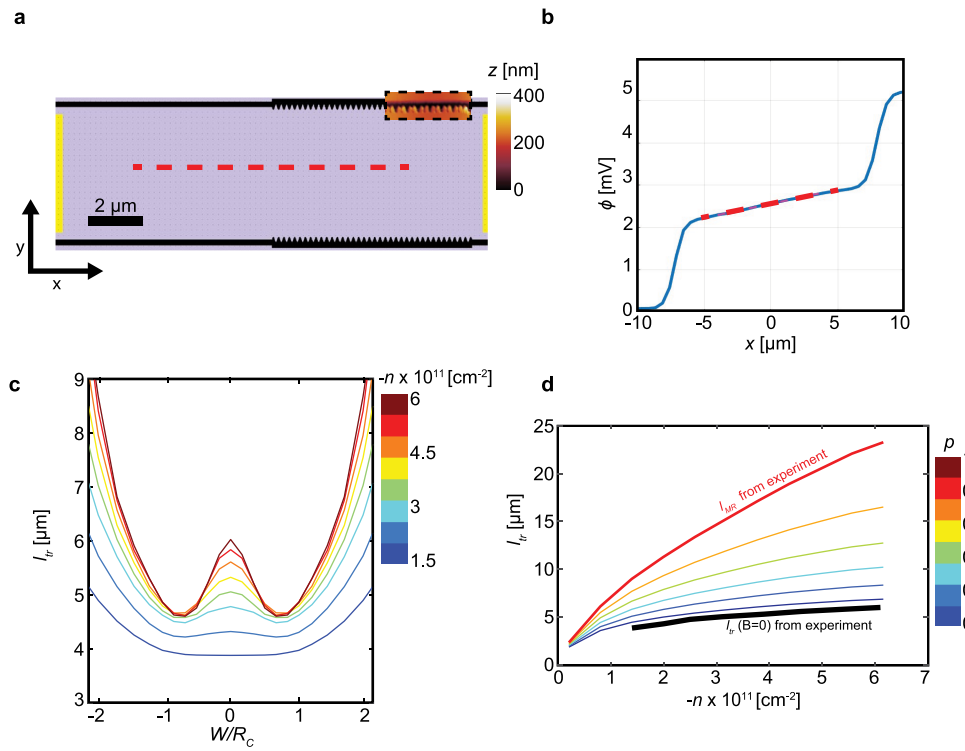
**Peer review information** *Nature* thanks Klaus Ensslin, Boris Narozhny and the other, anonymous, reviewer(s) for their contribution to the peer review of this work.

**Reprints and permissions information** is available at <http://www.nature.com/reprints>.



**Extended Data Fig. 1 | Relation between transport and momentum-relaxing mean free path across the phase diagram of flow regimes and the electron mobility.** **a**, Boltzmann calculation of  $l_{\text{tr}}$  versus  $l_{\text{MR}}$  and  $l_{\text{ee}}$ . The two-dimensional map shows the ratio of the finite-field-transport mean free path,

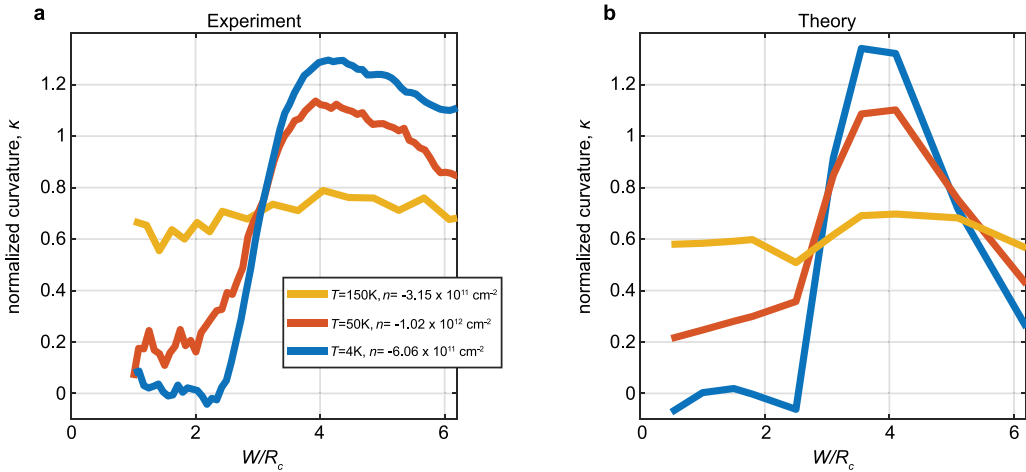
$l_{\text{tr}}(B) = h/[2e^2(\pi|n|)^{1/2}\rho_{xx}(B)]$ , and the bulk mean free path,  $l_{\text{tr}}/l_{\text{MR}}$ , calculated using Boltzmann theory at  $W/R_c = 3.2$  for a channel with diffusive walls, as a function of  $l_{\text{ee}}/W$  and  $l_{\text{MR}}/W$ . **b**, Electron mobility  $\mu$  measured with scanning SET, equivalent to the  $l_{\text{MR}}$  data presented in Fig. 1d.



**Extended Data Fig. 2 | Diffusivity of etched channel walls in the experiment.**

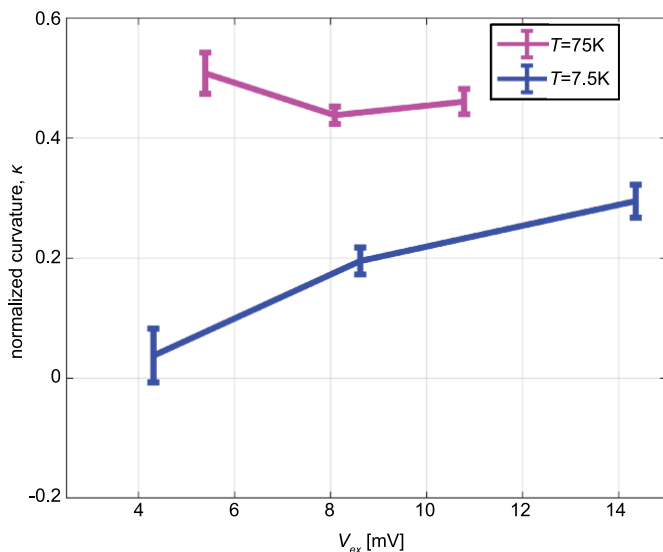
**a**, Illustration of a channel used to assess the diffusivity of etched walls by direct comparison to lithographically roughened walls. The walls of the left half of the channel are patterned with a typical straight-line pattern, whereas the right half is patterned with a saw-toothed pattern to introduce roughness. The region enclosed by the dashed box in the upper right is an AFM image of the etched walls. The red dashed line marks the spatial region spanning both wall patterns along which the potential drop is measured. **b**, Measured potential

drop along the centre of the channel (red dashed line in **a**). Away from the voltage steps at the contacts, the potential drops linearly across the device, with no observable change in slope when the walls transition from straight line to saw-tooth etches. **c**, Zoom of magnetoresistance data from Fig. 1c plotted as  $I_{tr}(B)$  for varying density. At the transition where the double peak disappears,  $I_{tr}(B=0) \approx W/(1-p)$ , allowing estimation of specularity  $p$ . **d**, Theoretical scaling of  $I_{tr}(B=0)$  with  $n$  for varying  $p$  superimposed with the experimental data (bold black line), indicating that  $p$  is nearly zero (fully diffusive walls).

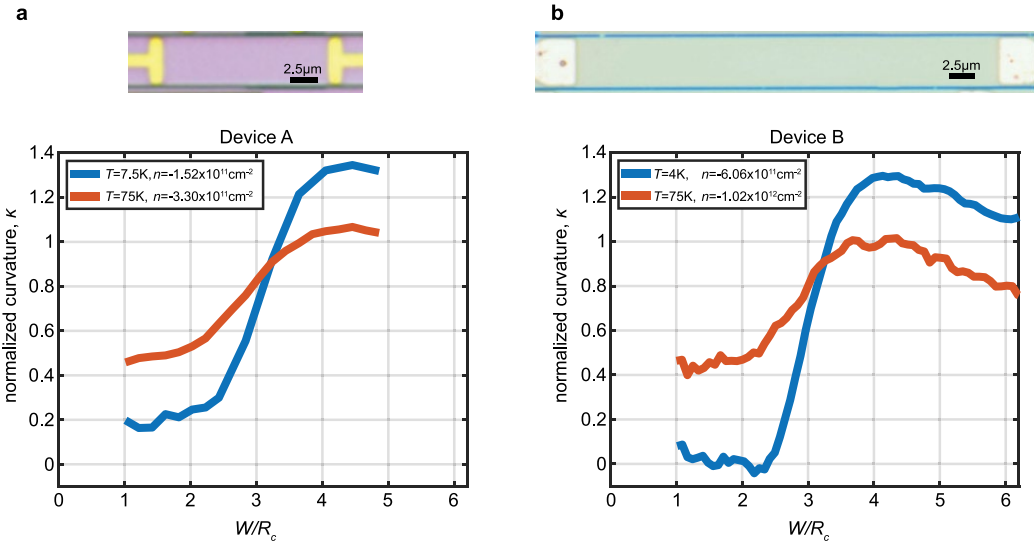


**Extended Data Fig. 3 | Dependence of Hall field profile curvature on magnetic field.** **a**, Measured traces of  $\kappa$ , extracted from  $E_y$ , using a fit to the centre of the channel, as a function of magnetic field plotted in units of  $W/R_c \propto B$ . The blue trace is measured at  $T = 4\text{ K}$  and hole density of  $n = -6.06 \times 10^{11} \text{ cm}^{-2}$  on device B (see Methods and Extended Data Fig. 5). The orange trace is measured at  $T = 50\text{ K}$  and  $n = -1.02 \times 10^{12} \text{ cm}^{-2}$  on device B, and the yellow trace is measured at  $T = 150\text{ K}$  and a hole density of  $n = -3.15 \times 10^{11} \text{ cm}^{-2}$  on

device A, which is the device used throughout the main text. Two distinct regimes are apparent: Below  $W/R_c \approx 2$ , the curvature is nearly independent of  $W/R_c$ , whereas above it varies noticeably, acquiring large values. **b**, Curvature as a function of  $W/R_c$  extracted from a Boltzmann simulation of  $E_y$  as described in the main text. Coloured curves correspond to values of  $l_{\text{MR}}$  and  $l_{\text{ee}}$  that best match experiment. This figure verifies that by imaging at  $W/R_c = 1.3$  as in the main text, the profiles are not influenced by the magnetic field.


**Extended Data Fig. 4 | Dependence of Hall field profile curvature on voltage excitation.**

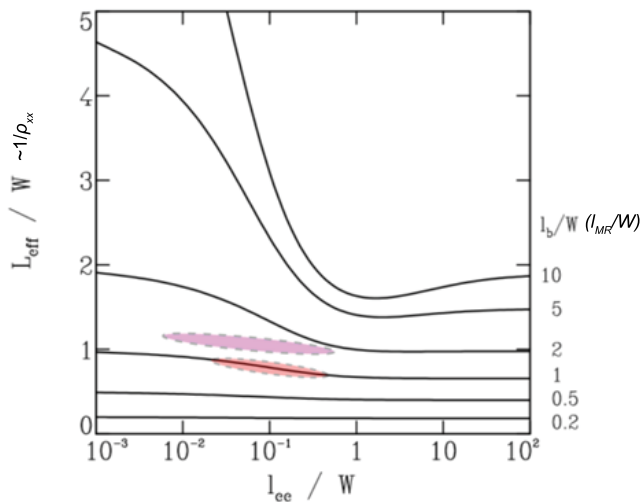
$\kappa$ , the normalized curvature of  $E_y$ , is plotted as a function of the excitation amplitude  $V_{\text{ex}}$  applied between the contacts of the channel. Error bars correspond to standard deviation of  $\kappa$  from the least-squares fit of a parabola to the data. The blue trace shows  $T = 7.5\text{ K}$  and  $n = -1.5 \times 10^{11} \text{ cm}^{-2}$ ; the purple trace shows  $T = 75\text{ K}$  and  $n = -3.3 \times 10^{11} \text{ cm}^{-2}$ . This plot verifies that by choosing appropriate values for the excitation, as was done for the experiments in the main text, electron heating effects are negligible.



**Extended Data Fig. 5 | Comparison of Hall field profile curvature for different devices.** **a**, Top, optical image of graphene device (device A) patterned into the geometry of a channel, with  $W = 4.7\text{ }\mu\text{m}$  and  $L = 15\text{ }\mu\text{m}$ , studied in the main text. Bottom, normalized curvature of  $E_y \kappa$ , measured as a function of  $W/R_c$ . **b**, Top, optical image of an additional graphene device

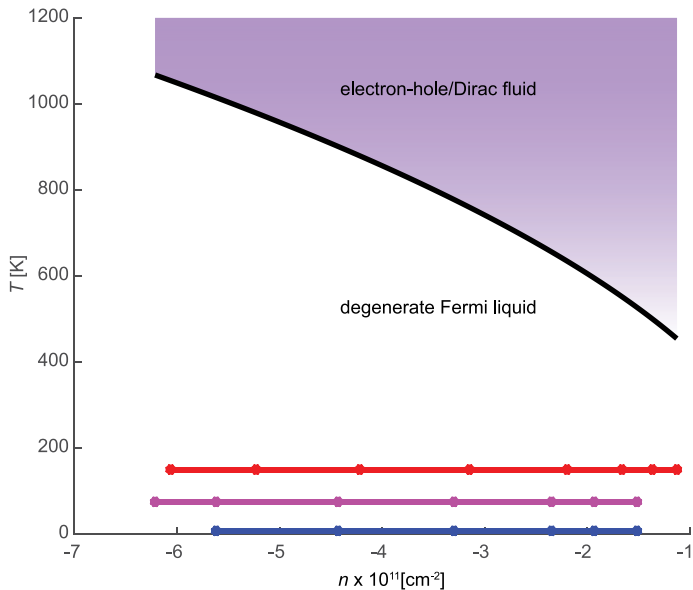
(device B) used for similar measurements, with  $W = 5\text{ }\mu\text{m}$  and  $L = 42\text{ }\mu\text{m}$ . This device was measured in a separate cryostat with a different scanning microscope and different SET. Colour differences between optical images are due to lighting conditions. Bottom,  $\kappa$  versus  $W/R_c$  measured for device B, showing a result highly consistent with that in **a**.

## Article



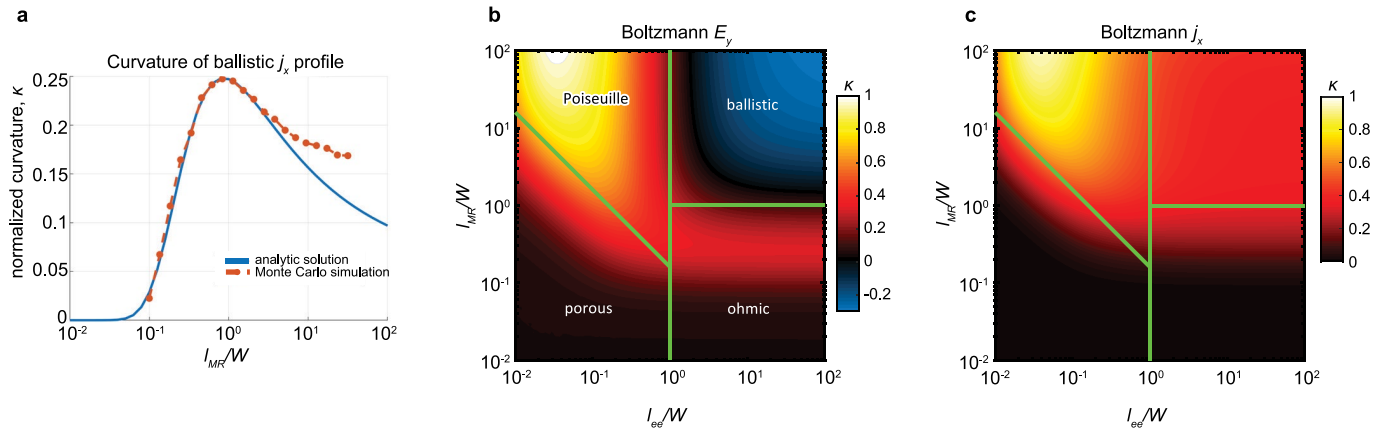
**Extended Data Fig. 6 | Distinguishing electron flow regime from transport.**

The graph shows the dependence of  $L_{\text{eff}}/W$ , which is inversely proportional to the resistivity, on  $l_{\text{ee}}/W$ , for fixed values of  $l_b/W = l_{\text{MR}}/W$ . The purple- and red-coloured regions correspond to the parameter ranges of our experiment for  $T=75\text{ K}$  and  $T=150\text{ K}$ , respectively. It is evident from these curves that the dependence of the resistivity on  $l_{\text{ee}}/W$  is fairly weak when  $l_{\text{MR}}/W$  is not much larger than 1. Figure reprinted with permission from de Jong and Molenkamp<sup>2</sup>; copyright 2019 by the American Physical Society.



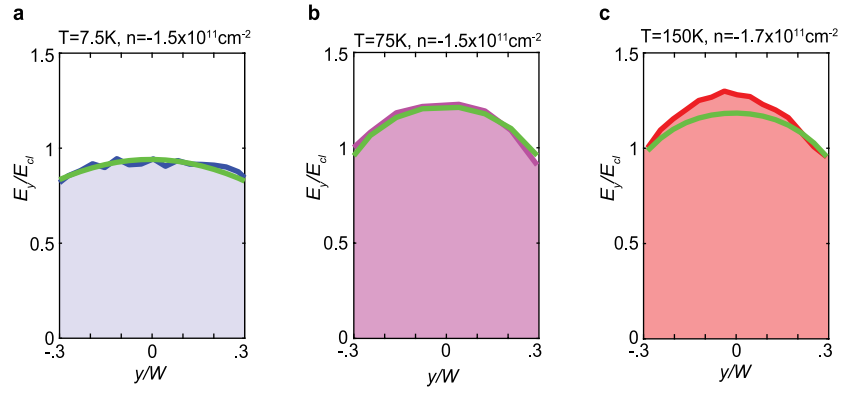
**Extended Data Fig. 7 | Phase diagram demonstrating that the experiment falls within the Fermi liquid regime.** The black line shows the equality  $E_F = k_B T$ , which separates the temperature–density plane into two distinct regimes. Above this line is the Dirac fluid regime in which electrons and holes are both present and thus electron–hole scattering must be considered. Below this line is the degenerate Fermi liquid regime in which only one charge carrier is present. The blue, purple and red lines correspond to the experiments presented in Fig. 4 at  $T = 7.5\text{ K}$ ,  $T = 75\text{ K}$  and  $T = 150\text{ K}$ , respectively, and show that our experiments are categorically within the Fermi liquid regime.

# Article



**Extended Data Fig. 8 | Curvature of ballistic  $j_x$  and comparison of theoretical  $E_y$  and  $j_x$  across phase diagram.** **a**, Curvature of ballistic current profile versus  $I_{\text{MR}}/W$ . The analytic solution (blue curve) is based on de Jong and Molenkamp<sup>2</sup> and the red curve is a Monte Carlo billiard ball simulation result. The two methods agree perfectly until  $I_{\text{MR}}$  exceeds the channel length used in the billiard ball simulation, beyond which the solutions begin to deviate. **b**, Curvature  $\kappa$  of  $E_y$ , as in Fig. 4b, calculated by Boltzmann simulation (see Methods), as a function of  $I_{\text{ee}}/W$  and  $I_{\text{MR}}/W$  for  $W/R_c = 1.3$ . Curvature is calculated over the centre of the channel. Green lines divide the panel into flow

regimes as in Fig. 4b. **c**, Curvature  $\kappa$  of  $j_x$ , extracted from the same simulation as in **a**. For  $j_x$ , the curvature in the ballistic regime is essentially constant at  $\kappa \approx 0.31$  and so the curvature of  $j_x$  is less discriminating between the hydrodynamic and ballistic regimes than the curvature of  $E_y$ , which becomes negative. In the other regimes, the curvatures of  $j_x$  and  $E_y$  are very similar, and the differences between them diminish as each of the length scales becomes much smaller than  $W$ . In the hydrodynamic regime the curvature saturates on the maximal possible value for a strictly parabolic profile, and in the porous regime it follows the length scale  $D_v = \frac{1}{2} \sqrt{I_{\text{MR}} I_{\text{ee}}}$  as expected.



**Extended Data Fig. 9 | Comparisons of representative imaged  $E_y$  profiles to the Boltzmann simulated profiles.** Boltzmann simulation profiles are plotted in green, whereas the experimental data is plotted with the same colour

scheme as in main text based on temperature (blue for  $T=7.5\text{ K}$ , purple for  $T=75\text{ K}$  and red for  $T=150\text{ K}$ ). The field  $E_y$  is normalized as in the main text by the classical Hall field  $E_{cl}=(B/ne)(I/W)$ .